

# Latest aviation applications of LIDAR at the Hong Kong International Airport

P.W. Chan

Hong Kong Observatory, Hong Kong, China

## Abstract

Doppler Light Detection And Ranging (LIDAR) systems have been used operationally by the Hong Kong Observatory (HKO) in the alerting of low-level windshear at the Hong Kong International Airport (HKIA). The operational algorithm is mainly based on the headwind profiles measured by the LIDARs along the flight paths of the aircraft, and significant headwind changes are identified automatically using a novel algorithm. This paper provides an update about the latest developments of the application of LIDAR for the alerting of windshear, which could be disastrous to the operation of the aircraft near the ground. Various kinds of methods are considered, including: (i) identification of fluctuating wind structures from the 2D winds retrieved from the LIDAR; (ii) calculation of windshear hazard factor based on the headwind data from the LIDAR; and (iii) calculation of turbulence intensity profiles using the LIDAR's glide path scans. Based on the limited datasets as presented in this paper, it turns out that the various methods all show skills in capturing the low-level windshear reports from the pilots. Future studies would include, among others, the optimal combination of windshear alerts from the various methods to achieve the best performance in the windshear alerting service.

## 1. Introduction

Aviation safety could be affected by such hazardous weather as low-level windshear and turbulence. In Chan (2010a), some applications of Doppler Light Detection And Ranging (LIDAR) systems at the Hong Kong International Airport (HKIA) for monitoring the disastrous weather conditions are described. It demonstrated that the radial velocity data from the LIDAR are useful in the aviation meteorological applications. They have been used, among others, in real-time monitoring of low-level windshear through the LIDAR Windshear Alerting System (LIWAS, with the algorithm called GLYGA, see Shun and Chan [2008]).

There have been on-going developments in the application of the two LIDAR systems at HKIA, one serving the north runway (the north-runway LIDAR) and another serving the south runway (the south-runway LIDAR). This paper summarizes the latest development efforts, including:

- (i) Monitoring of low-level windshear based on analysis of Lagrangian Coherent Structure (LCS);
- (ii) Monitoring of low-level windshear through the calculation of an alternative windshear hazard factor that is mainly used onboard the aircraft, namely, F-factor; and
- (iii) Studying the performance of LIDAR-based turbulence intensity and its use in the monitoring of low-level windshear.

## 2. Identification of LCS structure

The monitoring of airflow near HKIA using the LIDAR's radial velocity data is a kind of Eulerian descriptions of the flow field. It has recently been established that, such descriptions, inefficient and somewhat arbitrary at best, could lead to serious flaws as instantaneous streamline sketches is not an objective representation of actual particle motion in an unsteady flow. Lagrangian analyses, however, provide frame-independent description when the flow field is not evolving too quickly, and certain trajectories of an unsteady flow persist with coherent motion over some period of time. The method analyzes the relative motion of fluid particles in the Lagrangian frame. In this framework, LCSs are identified as distinguished sets of fluid particle trajectories that attract or repel nearby trajectories at locally the highest rate in the flow. Practically, they are identified using finite-domain finite-time Lyapunov exponents (FDFTLE) method. Technical details of the method can be found in Tang et al. (2011).

In the airport region, sometimes a long and distinct ridge of updraft is persistent as an organizing structure. We show the evolution of this updraft between 14:36 UTC and 14:41 UTC, 19 April 2008, in Figure 1, at 150 second intervals. This ridge of updraft originates downwind of Lin Fa Shan, a mountain on Lantau Island to the south of HKIA. The ridge could correspond to the merging of gap flows on the two flanks of the mountain peak, leading to convergence and updraft when they meet. Unlike other coherent structures which either stay in the vicinity of mountain topography or move with the background flow and quickly dissipate, this ridge is larger in scale and stay longer in time. More importantly, this ridge is transversal to the

runway corridor, where many flights passed through. In Figures 1(a), (b), and (c), the line of sight (LOS) velocity is shown. Not much of the velocity structures can be directly inferred from these plots. The FDFTLE plots in Figures 1(e), (f), and (g), however, reveal the updraft structure. In addition, we plot the Hovmoller diagram of the LOS velocity (Figure 1(d)) and the backward-time FDFTLE (Figure 1(h)) at 5 km range between 45 - 105 degrees azimuth and 14:00 - 16:00 UTC to study the relation between LCS and LOS velocity for this specific updraft. Since the updraft structure is transversal to the arc 5 km from LIDAR, we locate its time evolution in terms of the change in azimuthal angles where the ridge appears. We plot the evolution of the azimuthal angle in black in both Hovmoller diagrams. It is seen that this curve corresponds to a sharp transition of LOS velocity at 5 km range from the LIDAR. Above the curve, the flow is to the right of the ridge, and move faster towards the LIDAR. Below the curve, the flow is to the left of the ridge and move slower. As such, the converging flow gives rise to the persistent ridge in our analyses.

The correlation between LCS and aircraft response is also studied. In the top panels Figure 2(a) and (b), we superimpose the aircraft trajectory with the HKIA topography and the FDFTLE fields extracted at the time when the aircraft reaches the runway threshold (13:46 UTC, 19 April 2008). The black isocontours indicate the topography near the airport. The color maps show forward-time and backward-time FDFTLE, respectively. The two thick white lines in the center of the domain are the runway strips. The two black dots next to the runways show locations of the LIDARs. The aircraft landing trajectory from the east is shown as the thin black line aligned with the runway strips. We see that several terrain induced LCS intersect the landing trajectory and appear to have an impact on the approaches.

In the centre panels, in Figures 2(c) and (d), we compare LCS with on-board data. The most important on-board data relevant to our analysis is the measured vertical acceleration of aircraft during the landings as they measure the response of the aircraft to aerial disturbance. In the absence of any such disturbance, the perturbed vertical acceleration of the plane is zero, resulting in a constant speed of descent. The vertical acceleration data is given in units of  $g$  ( $9.81 \text{ m/s}^2$ ). Therefore, acceleration values above  $1g$  indicate updrafts and values below  $1g$  indicate downdrafts.

Because the aircraft measures data at higher frequency as compared to LIDAR, small scale variations make a direct comparison between LCS and vertical acceleration challenging. We filter

out some of these variations by requiring net acceleration to be larger than  $0.05g$  to qualify as significant air disturbances. In Figures 2(c) and (d), net acceleration is plotted as the black curve, in units of  $g$ . The two black dashed lines show references of  $\pm 0.05g$ ; significant updrafts and downdrafts are above or below the two dashed lines.

To compare these air disturbances with LCS, we interpolate the FDFTLE fields along the landing trajectory, at times when the airplane reaches the same locations (thus the interpolation is based on a time evolution of the LCS). Especially in Figure 2(c), for ease of comparison between downdrafts and LCS, we plot negative values of the forward-time FDFTLE interpolation, so downdrafts can be directly compared to troughs of FDFTLE. We also filter out the less significant values of FDFTLE (those less than 0 indicating contraction) by setting them equal to 0, and thus highlight the important LCS for comparison. Since the airplane landing is usually between the 1.4 degree and 3.0 degree LIDAR cones, we show interpolation of FDFTLE based on both elevation angles. The red curves in Figures 2(c) and (d) are based on 1.4 degree scans and the blue curves are based on 3.0 degree scans. Also, for clarity, we have shifted the red curves by  $-0.4$  and blue curves by  $0.4$ . The peak-peak and trough-trough correspondence indicate correlation of LCS and air disturbances.

Finally, at the bottom panels, we show comparisons between LIDAR scan cones and the airplane altitude as it approaches the runway. Since the runway corridor is generally between the two LIDAR cones (until the airplane touches down at runway threshold, when it descends below the 1.4 degree scan), locations of the aircraft relevant to the LIDAR cones indicate which scan is more reliable. The two LIDAR cones are shown in red, along with the airplane altitude in black. For this approach, the airplane decreases altitude towards the runway threshold at about 1 km (0 km is the location of the north-runway LIDAR). At the runway threshold it is still quite high and the aircraft also experiences an updraft. The airplane is pulled up to conduct its second approach. Indeed, it is observed that the aircraft experience several updrafts, both from the vertical acceleration profile in the centre panels and the dipping-flattening patterns in its altitude.

To aid comparison, we use black vertical lines to align air disturbances which are correlated to LCS. For example, in Figure 2(c), we first locate troughs of (negative) forward-time FDFTLE. Nearby these troughs, especially the significant ones, we observe strong downdrafts. We draw vertical lines when such correspondence exist and extend them to the top and bottom panels. It is seen that at the top

panels the vertical lines can be associated with airplane trajectories intersecting with the FDFTLTLE ridges. At the bottom panels these reference lines can also be associated with several disturbances to the airplane descending trajectories. We do not require a precise match in location since the LIDAR scans and on-board measures are independent sets of data and do not match precisely. As long as the FDFTLTLE extrema and the significant air disturbances are fairly close by, we claim that there is a match between the two peaks/troughs. It is seen in Figure 2, especially in the centre panels, that almost all FDFTLTLE extrema can be associated with significant air disturbances. The reverse argument is not true as airplane data has higher frequencies and thus has more variations than LCS.

### 3. Windshear hazard factor (F-factor)

F-factor is defined as follows:

$$F = \frac{1}{g} \frac{d}{dt} U_x - \frac{w}{V_a} \quad (1)$$

where  $U_x$  is the tailwind along the glide-path direction  $x$ ,  $t$  is the time,  $w$  the vertical wind velocity,  $V_a$  the aircraft airspeed, and  $g$  the acceleration due to gravity. Windshear may be alerted if F-factor reaches  $\pm 0.105$  for, e.g. microburst.

The concept employed in the derivation of the F-factor is the total aircraft energy and its rate of change. The total aircraft energy is simply the sum of the air-mass relative kinetic energy and the internal potential energy. Details of the derivation could be found in Hinton (1993). From Equation (1), it could be seen that a positive F-factor acts to decrease the energy state of the aircraft: the F-factor is positive for a descending air mass (vertical velocity less than 0) and a wind field accelerating in the direction of the glide path. In the absence of air-mass vertical motion, performance-decreasing shears act to decrease the energy state of the aircraft, whilst performance-increasing shears act to increase the energy state.

In the present study, the vertical acceleration term of (1) is not considered, and F-factor is taken to be the gradient of headwind along the flight path. The headwind data are provided by the LIDAR measurements. The resulting F-factor profile is compared with that obtained from the Quick Access Recorder (QAR) data of the aircraft.

Two examples of LIDAR-based F-factor, with the inclusion of aircraft response based on a B-747 simulator, are considered for two typical cases of windshear at HKIA. The first example is a sea breeze case in winter time. Moderate to fresh

easterly winds prevailed over the airport area in the daytime of 15 January 2010. With prolonged solar heating of the ground, westerly sea breeze appeared to the west of HKIA. The radial velocity image for the conical scan of the south runway LIDAR with an elevation angle of 3.2 degrees is shown in Figure 3(a). Though westerly sea breeze only affected the glide path to the west of the south runway, weaker easterly winds were recorded beyond about 2 nautical miles to the west of the north runway as a result of sea breeze. From the data collected on a B777 aircraft landing at the north runway from the west (runway corridor 07LA) at 03:51 UTC on that day, the headwinds were 8 to 10 m/s from the runway threshold to 1 nautical mile away, dropping to 1 to 2 m/s at 2 nautical miles away. This headwind change (up to about 8 m/s) constituted significant windshear to the landing aircraft. In fact, the pilot of this aircraft reported the encountering of significant windshear with a headwind gain of 15 knots, which was consistent with the LIDAR observations.

The F-factor profile calculated from the LIDAR data is shown in Figure 3(b). It could be seen that there are more significant peaks of F-factor in between 1 and 2 nautical miles away from the runway threshold. The LIDAR-based F-factor profile basically has the same shape as the QAR-based profile. The peak in the F-factor profile reaches a value of about -0.09, which is less in magnitude than the conventional alerting threshold of -0.105. As such, it appears that for alerting low-level windshear other than microburst, a lower alerting threshold may be necessary.

Another typical example of low-level windshear at HKIA is shown in Figure 4(a). The LIDAR data show that a fresh to strong east to southeasterly airstream prevailed in the vicinity of HKIA. From the upper-air ascent in Hong Kong at 00 UTC, 5 February 2019 (not shown), a temperature inversion of about 2 degrees could be found between 500 and 600 m above mean sea level. The prevailing easterly airflow was disrupted by the terrain of Lantau Island, which has peaks rising to about 1000 m above mean sea level with valleys as low as 400 m in between. From the LIDAR's velocity image in Figure 4(a), the terrain disruption resulted in reverse flow of opposite wind direction to the background easterly winds. An aircraft landed at the north runway of HKIA from the west (07LA) at 06:35 UTC, 5 February 2010. Its QAR data showed that the headwind was in the order of 8 - 12 m/s in the first couple of nautical miles away from the runway threshold, dropping to about 4 m/s between 2 and 3 nautical miles from the runway. The change in headwind constituted an event of significant windshear for the pilot. This is consistent with the pilot report of headwind change

of 15 knots on approach.

The LIDAR-based F-factor profile is shown in Figure 4(b). It appears to be similar to the F-factor profile as calculated from QAR data. Apart from the highest peak of F-factor value from QAR data at about 4 nautical miles away from the runway threshold, higher F-factor values show up in both the LIDAR-based and the QAR-based profiles in between 2 and 3 nautical miles away from the runway. The maximum value (in magnitude) is about -0.06. Once again, this is smaller than the conventional alerting threshold of -0.105 and thus the alerting of low-level, terrain-induced windshear may require a lower threshold.

The relative operating characteristics (ROC) curves for positive and negative peak values of F-factor over the two mostly used arrival runway corridors 07LA and 25RA (i.e. landing at the north runway of HKIA from the east) are shown in Figure 5. They are based on the balancing between the hit rate (or POD, the probability of detection) and the alert duration (as percentage of time of the study period). It could be seen that, in general, the negative peak values are more skillful than the positive peak values. Moreover, the LIDAR-based F-factor alerts are more skillful over 07LA than 25RA. For negative peak of F-factor over 07LA, a hit rate of 85% could be achieved with an alert duration of about 8% of the time. This is comparable with the performance of the LIDAR-based headwind alerting algorithm (Shun and Chan, 2008). The corresponding alerting threshold is -0.05. This is consistent with the results obtained in the earlier discussion on case studies of LIDAR-based F-factor profile that a much lower alerting threshold than the conventional value of -0.105 may be required in the alerting of low-level windshear at HKIA.

#### **4. Application of LIDAR-based turbulence intensity values**

The LIDAR has the capability of capturing the rapid fluctuation of winds by providing radial wind data at 10 Hz. As a result, it could be used to calculate the turbulence intensity, which is expressed as the cube root of eddy dissipation rate ( $EDR^{1/3}$ ), the metric adopted by the International Civil Aviation Organization (ICAO) in the alerting of turbulence.  $EDR^{1/3}$  could be calculated from different scan patterns of the LIDAR. In Chan (2010b), the turbulence intensity is determined based on the radial wind velocity data obtained in the glide-path scans. This approach is particularly useful in the alerting of turbulence for the landing/departing aircraft at the airport because the scan strategy mainly focuses on data collection along the glide path. From preliminary results

presented in Chan (2010b), the  $EDR^{1/3}$  calculated from glide-path scans appears to have potential in the alerting of low-level turbulence of the arriving aircraft, by comparison with the pilot windshear reports and the turbulence data from the Windshear and Turbulence Warning System (WTWS) operated by the Hong Kong Observatory, for a number of typical cases of turbulence at HKIA. However, pilot reports are subjective in nature, and the  $EDR^{1/3}$  from WTWS is mainly based on ground-based anemometers which are far away from the glide paths of the aircraft. As a result, it is not sure if the turbulence intensity so calculated is indeed of sufficiently good quality for low-level turbulence alerting purpose.

In order to establish the alerting algorithm for low-level turbulence, it is crucial to collect high-quality turbulence data. To this end, the Observatory collaborated with Government Flying Service of the Hong Kong Government to equip a Jetstream 4100 fixed-wing aircraft with a set of meteorological equipment. This equipment could be used to provide three components of the wind at an accuracy of 0.5 – 1 m/s for straight and level flights at a frequency of 20 Hz. The use of this dedicated equipment makes it possible to obtain high-quality turbulence data in the arrival and departure runway corridors at HKIA. The aircraft-based turbulence is calculated using the method similar to that reported in Haverdings and Chan (2010). The turbulence data are taken as sky truth in assessing the performance of the LIDAR-based turbulence calculation algorithm.

The comparison results between the LIDAR-based and Jetstream-based  $EDR^{1/3}$  values are shown in Figure 6. The commonly used arrival runway corridors of HKIA, namely, 07LA and 25RA are considered. Following the turbulence reporting method as adopted in the US, the median values and the 95 percentile values of  $EDR^{1/3}$  are studied. It could be seen that the two datasets have very good correlation. The study period covers eight months in 2010 when data collections were made using the Jetstream aircraft, and thus it includes a variety of meteorological conditions and many seasons. The good correlation gives confidence about the quality of the LIDAR-based turbulence data. Study is underway to examine how the LIDAR-based turbulence intensity performs in capturing the pilot reports of moderate and severe turbulence, based on a much larger sample of reports than that in Chan (2010b).

Meanwhile, the use of LIDAR-based EDR in the alerting of windshear is studied because of the much larger sample size of windshear pilot reports than turbulence pilot reports. It has been suggested that it might be difficult for pilots to

differentiate between windshear and turbulence at times, as both refer to rapid fluctuations in the wind, especially for terrain-induced windshear which is the main cause of low-level windshear at HKIA. The performance of LIDAR-based EDR in capturing the low-level windshear is studied again using the ROC curve, namely, striking a balance between POD and alert duration as percentage of time of the study period. The period under consideration includes all days with pilot reports of windshear over 07LA and 25RA runway corridors in 2010. The resulting ROC curves are shown in Figure 7, including both the median and the maximum values of  $EDR^{1/3}$  along the flight path. It turns out that the LIDAR-based turbulence intensity shows skills in capturing the windshear. The ROC curves are all above the diagonal of the ROC diagram, though the optimum performance points are still rather far away from the upper left corner (ideal performance) of the diagram. Moreover, comparing with the performance of LIDAR Windshear Alerting System (with the algorithm GLYGA, please refer to Shun and Chan [2008]), the LIDAR-based EDR needs a longer period of alerting in order to achieve the same POD. Nonetheless, the results of the present study show that the LIDAR-based EDR has skills in capturing low-level windshear, particularly for 25RA with the ROC curves being closer to the ideal performance (upper left corner) in the ROC diagram. This opens up the possibility of combining GLYGA alerts and LIDAR-based EDR in the alerting of low-level windshear, which may achieve better results than the use of GLYGA alerts alone. This would be the subject of further study.

## 5. Conclusions

This paper provides an updated summary about various developments in the application of LIDAR in alerting disastrous weather for the assurance of aviation safety. In particular, the LIDAR data are analyzed in a number of ways, namely, the identification of LCS in the 2D retrieved winds, calculation of F-factor based on LIDAR headwind profiles, and calculation of EDR profile using the glide-path scan velocity data, in the capturing of low-level windshear. The various methods all show promising results in the windshear application. The next step would be how to combine the alerts, if any, as provided by these methods, together with the existing GLYGA alerts, to achieve the most optimal performance in warning the pilots about the occurrence of low-level windshear. In this regard, the alerts would be integrated using a well-developed prioritization scheme in order to get

the highest probability of detection of windshear reports (preferably at 90% or higher) with the shortest possible alert duration (as percentage of time of the study period), and the combined alerts must perform better than the existing overall windshear alerting service at HKIA, which mainly consists of GLYGA alerts and subjective windshear warnings issued by the human weather forecasters for non-rainy weather conditions. The eventual objective is to remove the need for human weather forecasters in issuing the subjective windshear warnings.

Other applications of LIDAR would be the topics of future studies as well. This includes the alerting of low-level turbulence based on the EDR calculated from the glide-path scans of the LIDAR. The visibility map generation algorithm based on backscattered data from the LIDAR is also under modification in order to achieve the best performance in various kinds of weather conditions, particularly those with larger amount of suspending water droplets in the air, in the monitoring of low visibility weather at HKIA.

## References

- Chan, P.W., 2010a: Latest developments of windshear alerting services at the Hong Kong International Airport. *Disaster Advances*, 3, 44 – 53.
- Chan, P.W., 2010b: LIDAR-based turbulence intensity calculation using glide-path scans of the Doppler Light Detection And Ranging (LIDAR) systems at the Hong Kong International Airport and comparison with flight data and a turbulence alerting system. *Meteorologische Zeitschrift*, 19, 549-563.
- Haverdings, H., and P.W. Chan, 2010: Quick access recorder data analysis software for windshear and turbulence studies. *Journal of Aircraft*, 47, 1443-1447.
- Hinton, D. A., 1993: Airborne Derivation of Microburst Alerts from Ground-based Terminal Doppler Weather Radar Information – a Flight Evaluation. NASA Technical Memo. 108990, 32 pp.
- Shun, C.M., and P.W. Chan, 2008: Applications of an infrared Doppler Lidar in detection of wind shear. *J. Atmos. Oceanic Technol.*, 25, 637 – 655.
- Tang, Wenbo, Pak Wai Chan, George Haller, 2011: Lagrangian coherent structure analysis of terminal winds detected by Lidar. Part I: turbulence structures. *J. Appl. Meteor. Climatol.*, 50, 325–338.

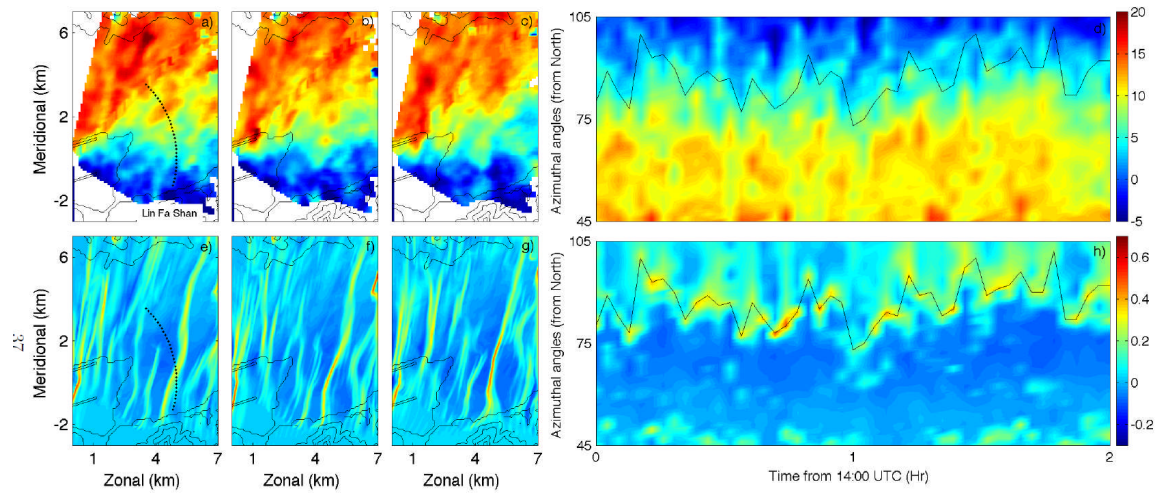


Figure 1 Ridge of updraft identified to the east of the airport, during the episode of spring tropical cyclone. (a), (b), and (c) are the LOS velocity output from LIDAR. It is not apparent that a ridge structure is present. (e), (f), and (g) are the backward-time FDFTLE. A long ridge of FDFTLE maxima is seen persistent over time, trailing Lin Fa Shan. The different times, from left to right for each pair of plots, are 14:36 UTC, 14:39 UTC and 14:41 UTC. (d) Hovmoller diagram of the LOS velocity at 5 km range between 14:00 - 16:00 UTC. The coverage is shown as the arc of black dots in (a). (h) Hovmoller diagram of the backward-time FDFTLE between 14:00 - 16:00 UTC. The FDFTLE maxima (on the persistent ridge) is connected by the black curve. This curve is also plotted in (d). It is seen that the ridge correspond to a rather strong change in LOS velocity.

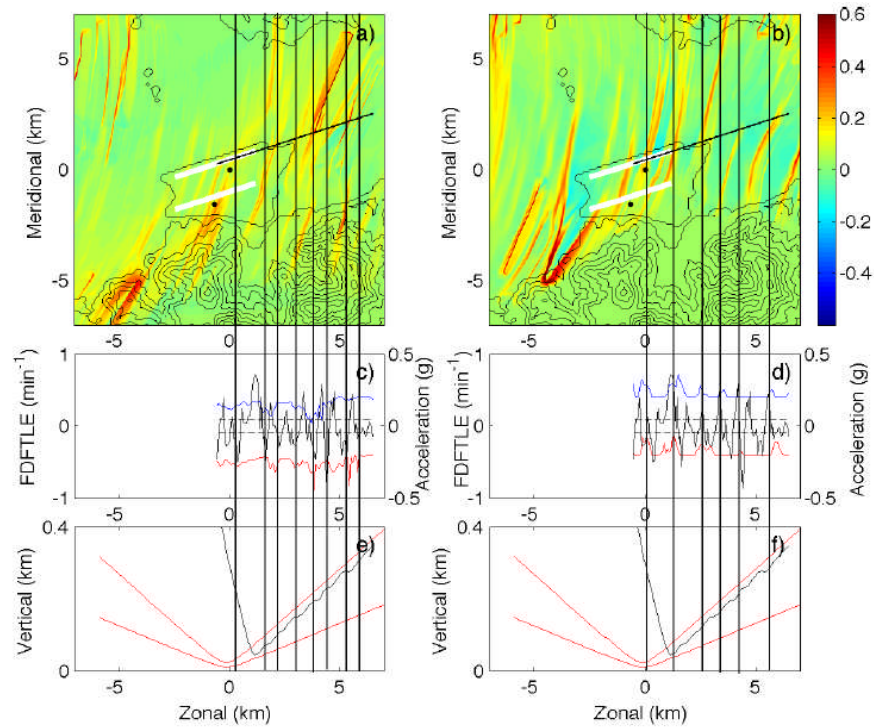
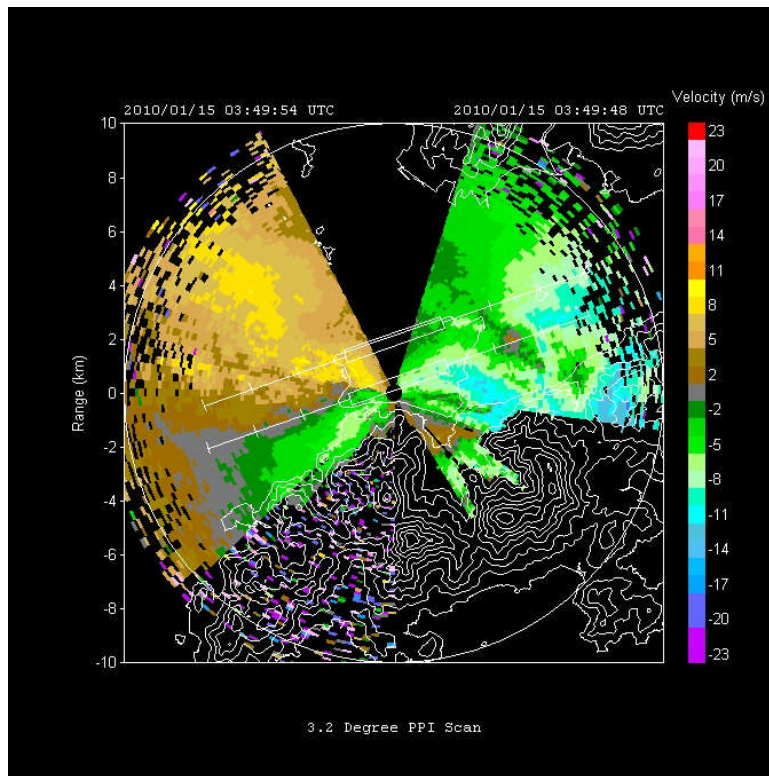
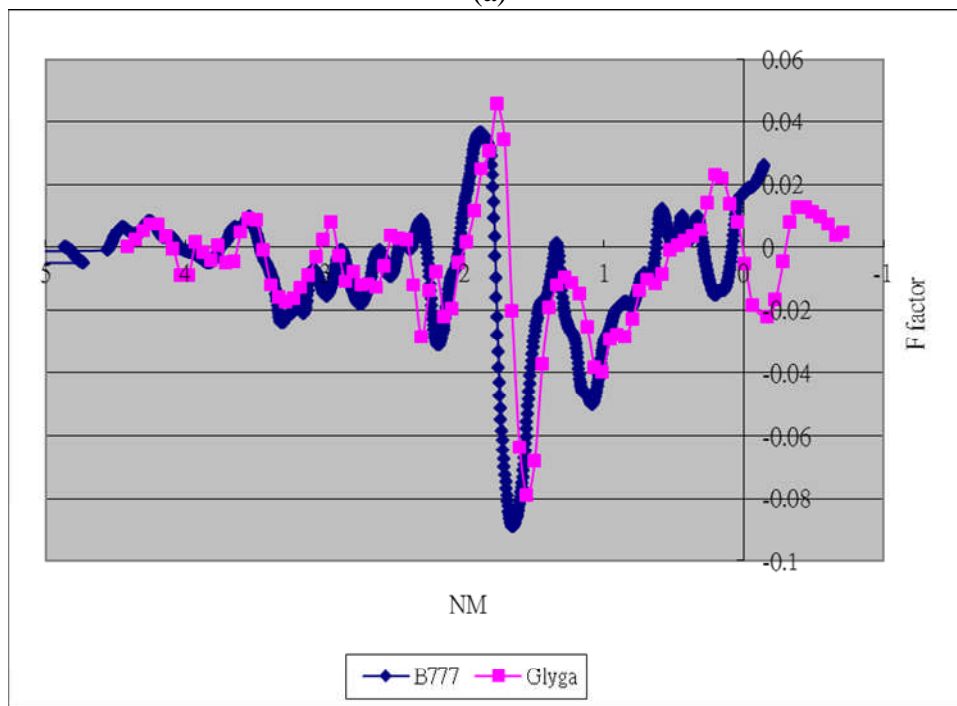


Figure 2 Airplane landing data compared to LCS for missed approach at 13:46 UTC, April 19th, 2008. (a) Approach superimposed on forward-time FDFTL based on the 1.4 degree scan. The black isocontours indicate terrain near HKIA. The thick white lines denote the two runways. The thin black line along the north runway denotes approaching trajectory. The black dots indicate positions of the LIDARs. (b) Approach superimposed on backward time FDFTL. All styles same as (a). (c) Comparison between vertical acceleration and FDFTL. Vertical acceleration measured onboard aircraft is shown in black, along with references of  $-0.05g$  and  $0.05g$ , plotted in dashed lines. The blue/red solid lines are the FDFTL generated from the 3.0 degree/1.4 degree scans and shifted by  $\pm 0.4$ , respectively. For ease of comparison, negative values of forward-time FDFTL are plotted. (d) Comparison between backward-time FDFTL and vertical acceleration. (e) and (f) show the airplane altitude as it approaches the runway in black, along with the 3.0 degree and 1.4 degree scan cones in red. The black vertical lines highlight places where LCS are correlated with vertical acceleration.

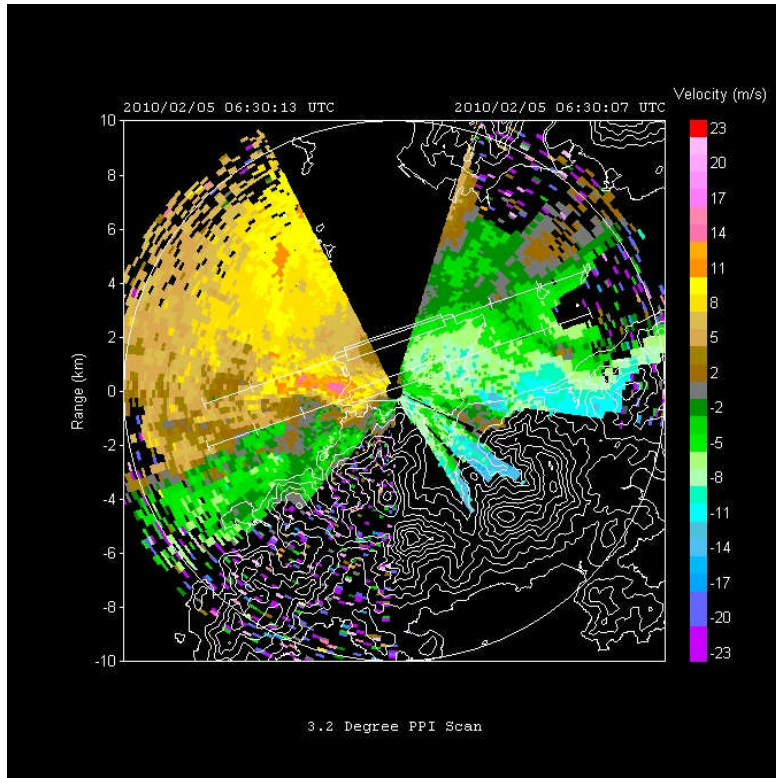


(a)

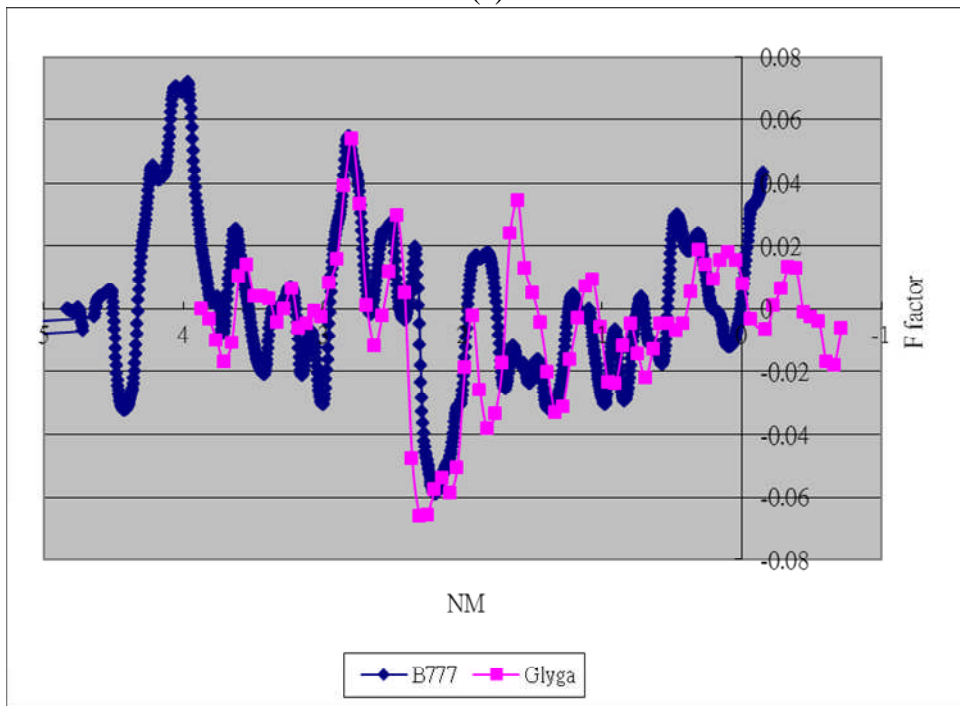


(b)

Figure 3 The 3.2-degree conical scan imagery of radial velocity of the south runway LIDAR at 03:50 UTC, 15 January 2010 (a) and the F-factor profile (F-factor as a function of distance from the runway threshold in nautical miles [NM]) from a B777 aircraft and LIDAR (GLYGA) at 0351 UTC of the same day (b).

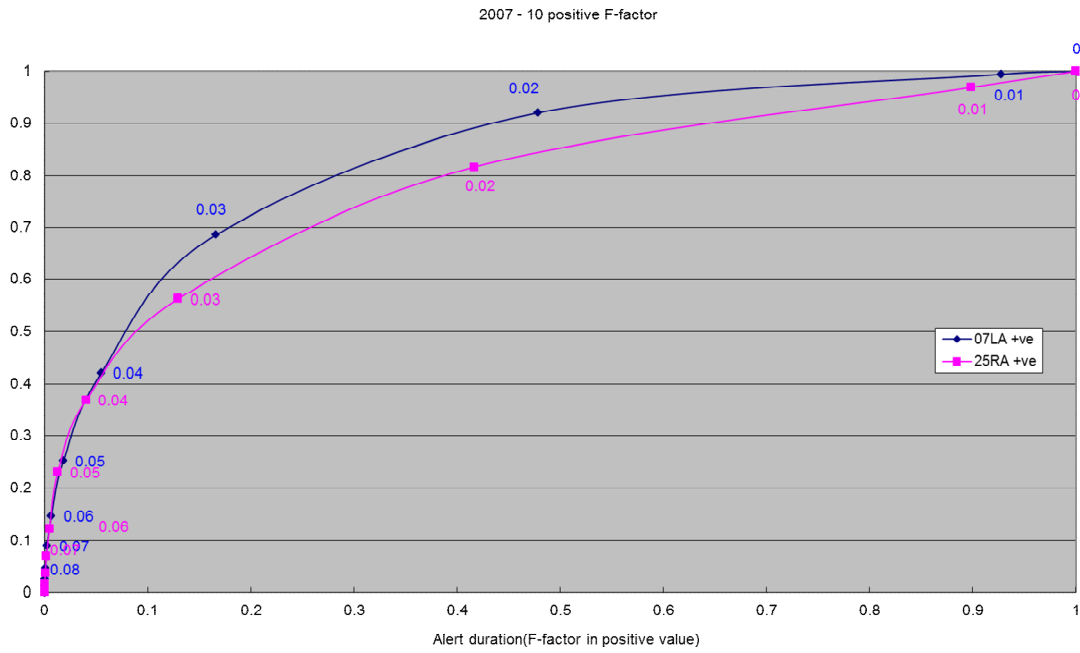


(a)

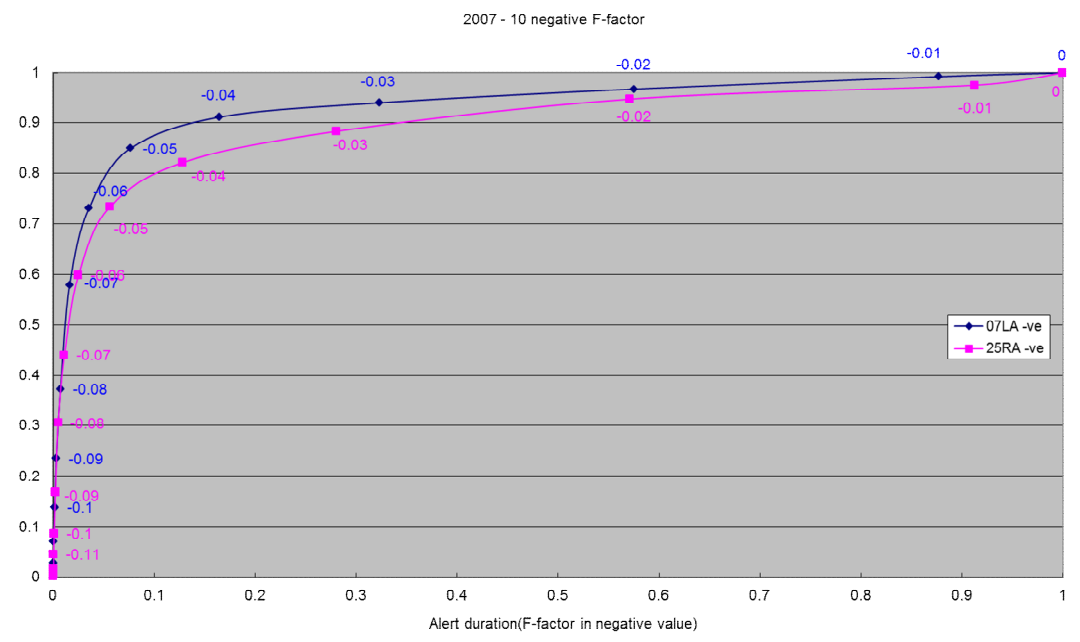


(b)

Figure 4 The 3.2-degree conical scan imagery of radial velocity of the south runway LIDAR at 06:30 UTC, 5 February 2010 (a) and the F-factor profile from a B777 aircraft and LIDAR (GLYGA) at 0635 UTC of the same day (b).



(a)



(b)

Figure 5 ROC curves for 07LA and 25RA in the study period: (a) using positive F-factor and (b) using negative F-factor. The threshold values are labelled against each data point. The y-axis refers to the hit rate of pilot windshear reports. The x-axis refers to alert duration as fraction of the time of the study period.

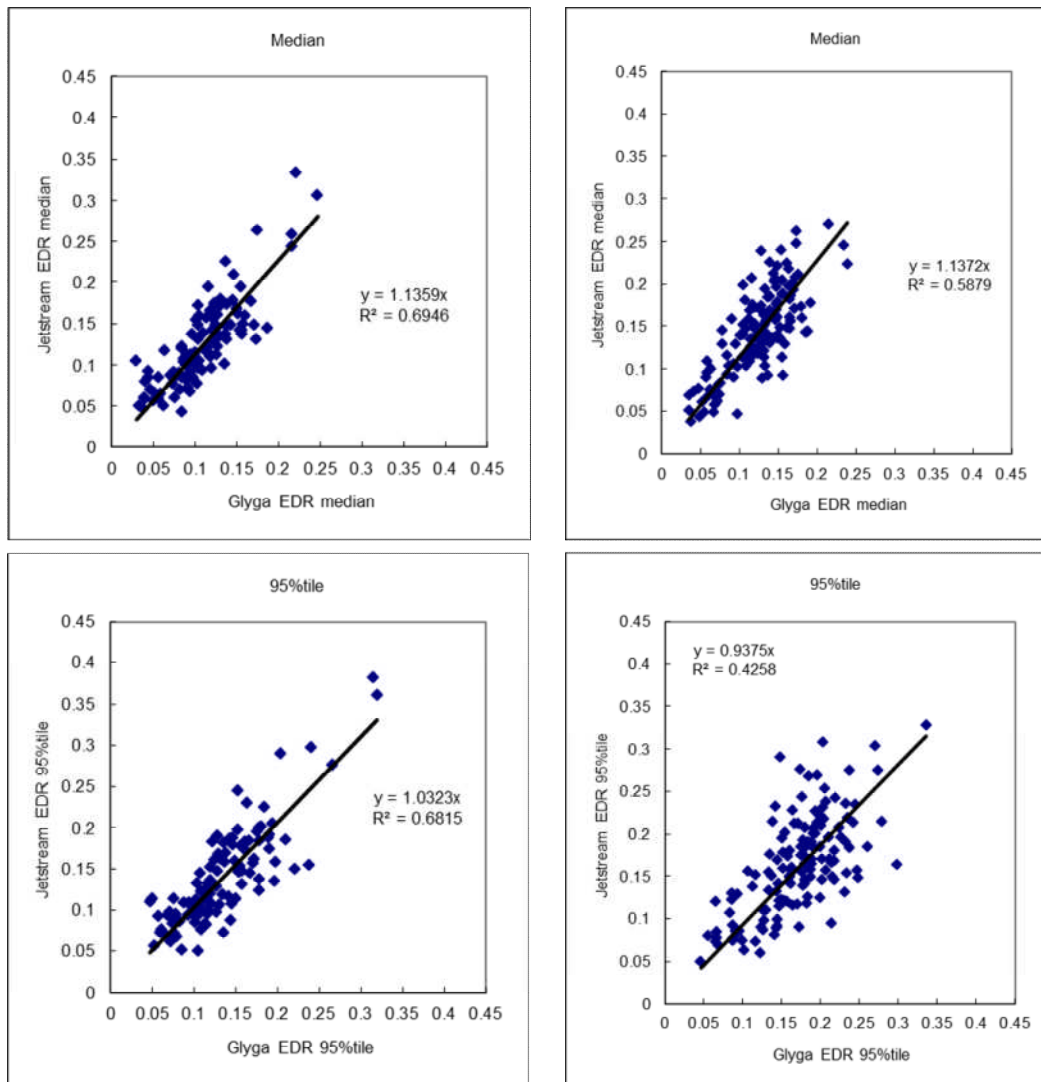


Figure 6 Scatter plots of  $EDR^{1/3}$  values from the Jetstream 4100 aircraft (y-axis) and those from the LIDAR (called GLYGA, x-axis). The top row refers to median values of  $EDR^{1/3}$  and the bottom row refers to 95 percentile values. The left panels are obtained from the aircraft landing at 07LA runway corridor, and right panels for landing at 25RA runway corridor.

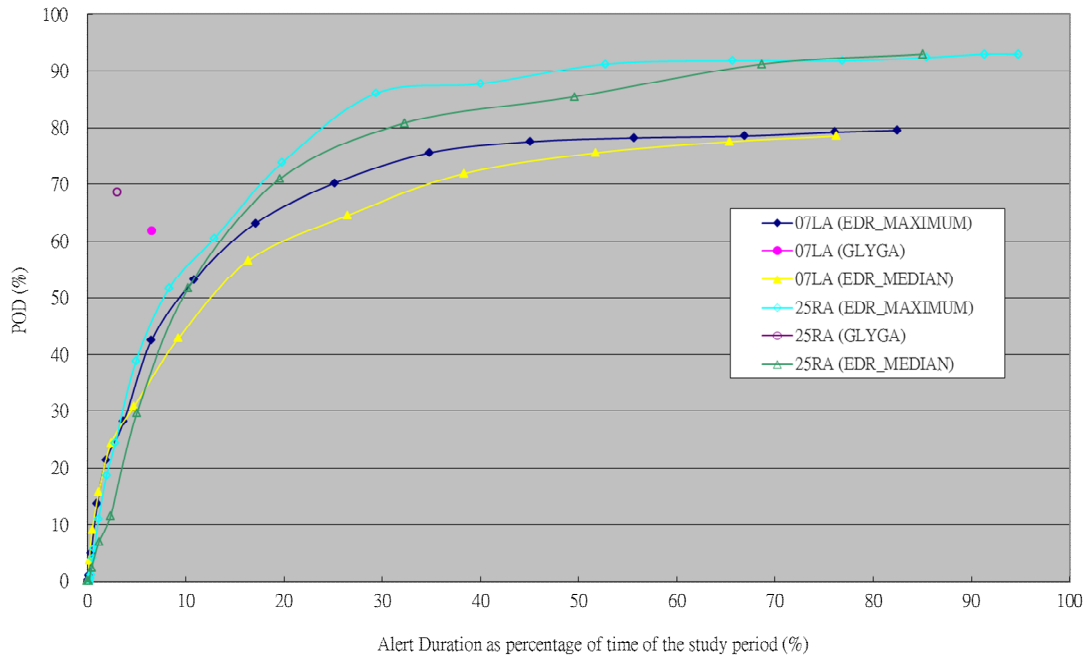


Figure 7 ROC curves for windshear detection based on median and maximum EDR values over 07LA and 25RA runway corridors. The data points refer to EDR<sup>1/3</sup> threshold from 0.06 (right) to 0.50 (left) with a step of 0.02. The performance of LIDAR windshear alerting system (GLYGA) is also given.